CHEMISTRY OF MATERIALS

Article

pubs.acs.org/cm

In Situ X-ray Absorption Spectroscopy Study of the Capacity Fading Mechanism in Hybrid $Sn_3O_2(OH)_2$/Graphite Battery Anode Nanomaterials

Christopher J. Pelliccione,*[,†,‡] Elena V. Timofeeva,[‡] and Carlo U. Segre[†]

[†]Department of Physics & CSRRI, Illinois Institute of Technology, 3300 South Federal Street, Chicago, Illinois 60616, United States

[‡]Energy Systems Division, Argonne National Laboratory, 9700 S. Cass Avenue, Lemont, Illinois 60439, United States

Supporting Information

ABSTRACT: In situ X-ray absorption spectroscopy (XAS) of an electrode material under electrochemical control has enabled a detailed examination of the capacity fading mechanism during charge−discharge cycling in a hybrid nanomaterial, $Sn_3O_2(OH)_2$/graphite, that is considered for use as a high-capacity lithium-ion battery anode. By the use of an original one-pot solvothermal synthesis technique, $Sn_3O_2(OH)_2$ nanoparticles were directly deposited on the surface of nanothin graphite and were charged/discharged in situ for several cycles while XAS spectra at the Sn K-edge were taken. Modeling of the collected extended X-ray absorption fine structure (EXAFS) spectra provides detailed information on the Sn−O, Sn−Sn, and Sn−Li coordination numbers and atomic distances for each charged and discharged electrode state. On the basis of electrochemical data and the changes in atomic arrangement deduced from the EXAFS fitting results, including the first unambiguous observation of Sn−Li near neighbors, a capacity fading mechanism is proposed that is different from widely accepted volume expansion for tin metal and tin oxides. Our experimental results suggest that atomic clusters of metallic tin surrounded by highly disordered Li_2O shells are formed on first charge. The metallic tin clusters participate in lithiation and delithiation on the following charge/discharge cycles; however, because of continued segregation of tin and Li_2O phases, the tin clusters eventually lose electrical contact with the rest of the electrode and become excluded from further participation in electrochemical reactions, resulting in reduced capacity of this anode material.

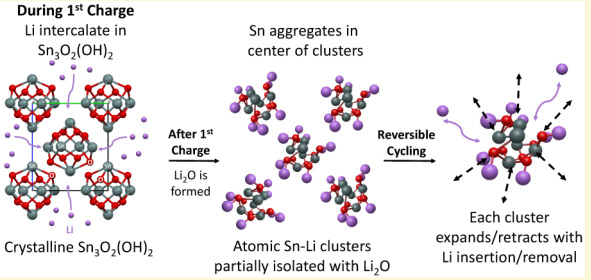

INTRODUCTION

Lithium ion batteries (LIBs) are the dominant power source for small-scale and portable electronic devices. Graphite is the most common anode material in such batteries because of its excellent cycle life and a reasonable compromise between Li insertion potential (between 0.1 and 0.2 V vs Li/Li^+) and specific capacity (theoretical capacity of 372 mAh/g).[1,2] However, for the next generation of LIBs to be utilized in electric vehicles, significant improvements need to be made in energy and power densities, as well as cycle life.[3] Metallic tin is an attractive alternative to graphite because of its high theoretical capacity (994 mAh/g) through formation of Li−Sn alloys up to $Li_{22}Sn_5$. However, this material suffers from large volumetric expansion of up to 260% during Li insertion.[4] It has been suggested that these volume expansions initiate cracking and fracturing of the material, limiting the overall electrical contact between tin particles and current collectors, thus quickly reducing the capacity to below 100 mAh/g after several cycles.[4] For tin to be a reasonable alternative to graphitic anodes, these destructive volumetric changes need to be mitigated. One of the approaches to help control the material's integrity during volumetric expansion is reducing the particle size, as it has been shown that smaller particles tend to maintain structural integrity due to surface tension and show increased cycle performance.[5−8] Another approach includes the use of tin oxides to help reduce stresses due to Li insertion, as on the first charge SnO_x is irreversibly converted to Li_2O and metallic tin.[9] The Li_2O provides structural support during metallic tin expansion on subsequent charge cycles. Kim et al.[10] used 5−10 nm crystalline $Sn_3O_2(OH)_2$ nanopowders embedded in an amorphous SnO_x phase. The initial reversible capacity of this material was 585 mAh/g and remained at ca. 500 mAh/g after 100 cycles, e.g., ca. 17% drop from the initial reversible capacity. These efforts have shown significantly improved cycling lifetime over metallic tin but are still far away from the cycle life and capacity required for commercial applications.

The use of nanoscale materials in a battery application makes it challenging to create good electrical contact to each nanoparticle. Carbon additives are typically used to improve electrical contact, but the tendency of nanoparticles to agglomerate results in limited effectiveness of such additives. Nanoparticles directly deposited on a carbon support resolves

Received: November 6, 2014
Revised: December 18, 2014
Published: December 19, 2014

DOI: 10.1021/cm504101h
Chem. Mater. 2015, 27, 574−580

this issue. Recently effort has been put forth in depositing nanoscale Sn or SnO_2 nanoparticles directly on graphite to help control volumetric expansion effects.[11−24] Zhang et al.[13] synthesized SnO_2/graphene anode material with a SnO_2 particle size of ca. 15 nm on the surface of graphene. These particles exhibit an initial reversible capacity of ca. 900 mAh/g that is reduced to ca. 600 mAh/g by the 50th cycle (i.e., a 33% drop). Yao et al.[19] created SnO_2/graphene nanocomposite (40 wt % SnO_2), with SnO_2 particle size of 4−5 nm, that exhibited an initial reversible capacity of 765 mAh/g but reduced to ca. 600 mAh/g by cycle 50 (22% drop) and to 520 mAh/g by cycle 100 (32% drop). In both studies the SnO_2/graphene nanocomposite had increased stability over SnO_2 nanoparticles not attached to carbon additives; however, the capacity drop is still observed and remains a significant obstacle for these type of anode materials to be considered as viable alternatives to graphite anodes.

Understanding the mechanism of lithiation/delithiation and capacity fading mechanisms in such anodes is crucial for successful development of high-capacity battery materials. Many attempts have been made to understand both the initial lithiation/reduction process in oxide materials producing Li_2O and metals and the process following this conversion in which the active elements (Sn, Si, etc.) directly interact with insertion/deinsertion of Li by using various characterization techniques such as X-ray diffraction (XRD),[25−27] X-ray absorption spectroscopy (XAS),[28−35] and more recently in situ transmission electron microscopy (TEM).[36,37] Rhodes et al.[27] conducted in situ XRD on 5 μm thin film tin electrodes. In a fully lithiated state, multiple crystal phases were detectable including Li_2Sn_5, $Li_{22}Sn_5$, and β-LiSn along with amorphous transitional phases. In a fully discharged state, metallic tin was observed. Nie et al.[36] observed real-time lithiation of ca. 20 nm diameter SnO_2 nanorods using a novel in situ TEM technique with resolution on the order of nanometers. They were able to resolve clear fronts for lithiation reactions and the evolution of amorphous domains of Li_2O, Sn, and Li_xSn scattered throughout the material.

It is clear that in high-capacity anodes both crystalline and amorphous phases, and their distribution, contribute to the capacity fading. Methods sensitive to both crystalline and amorphous phases are required for better understanding, and XRD is particularly limited in characterizing noncrystalline samples.

XAS is an element-specific technique, which can be used to probe only elements of interest. Unlike XRD, XAS is sensitive to all the atoms of the targeted type in the sample. This permits the collection of information about crystalline as well as amorphous phases that can be prevalent, especially with in situ or operando experiments. XAS, specifically X-ray absorption near-edge structure (XANES) spectroscopy and extended X-ray absorption fine structure (EXAFS) spectroscopy, are particularly powerful techniques to determine both local electronic and atomic structural changes in catalytic or battery applications. The XANES region is sensitive to electronic changes, specifically oxidation state, while the EXAFS region consists of local atomic structural information around the absorbing atom such as changes in coordination number, atomic identity, and atomic distances.

XAS has been previously utilized in studies of battery anodes and cathodes to better understand the lithiation/delithiation mechanisms. Mansour et al.[30] and Goward et al.[34]measured in situ Sn K-edge EXAFS spectra on tin composite oxide glass ($Sn_{1.0}Al_{0.4}B_{0.56}P_{0.4}O_{3.6}$) at various states of charge and discharge. On the basis of modeling of subsequent spectra, they concluded that on the first charge atomic-sized tin−metal clusters nucleate within the original glass matrix. Oxygen is retained in the immediate environment of tin clusters. Upon full lithiation a segregated Li−Sn−O nanocomposite is formed as the modeled Sn−O bond distance of 2.09 Å does not directly correlate to any tin oxide structure. In addition, Sn−Sn bond distance of 2.92 Å is close to the reported values for multiple LiSn phases such as Li_7Sn_3, Li_7Sn_2, Li_5Sn_2, and $Li_{13}Sn_5$; however, no direct evidence of Sn−Li neighbors is reported. It was also shown that, upon discharge, Sn−Sn neighbors are still present but the coordination numbers are reduced to between 1 and 2 Sn−Sn near neighbors, suggesting significant irreversible reduction of tin oxides to tin metal and highly dispersed metallic tin clusters. Chouvin et al.[32] investigated electronic and structural changes of SnO anodes with ex situ measurements at both the Sn L_I-edge and the O K-edge at various states of charge and discharge. The authors have shown that Sn−O pairs are present in all states, and in a fully charged state, Li−Sn alloys are present within the Li_2O matrix. They also suggest tin aggregation into metallic clusters upon first charge, which is consistent with the findings of Mansour and Goward.[30,34]

In this study we use the in situ XAS technique to investigate capacity fading of novel composite nanoparticles of $Sn_3O_2(OH)_2$ deposited onto graphite nanoplatelets ($Sn_3O_2(OH)_2$/GnP). The Sn K-edge EXAFS spectra in charged and discharged states were modeled to extract information on structural changes around tin atoms. We find results consistent with previously reported behavior;[30,32,34] however, we are able to incorporate Li−Sn structural models to quantify the lithiation in all charged and discharged states and suggest a capacity fading mechanism for this material, which is not based solely on volumetric destruction but rather on an overall limitation of the $Sn_3O_2(OH)_2$ crystal structure.

EXPERIMENTAL SECTION

$Sn_3O_2(OH)_2$/GnP Synthesis. $Sn_3O_2(OH)_2$/GnP composite nanomaterials were synthesized using a one-pot solvothermal technique. Oxidized commercially available GnP powder (0.08 g) was suspended in 50 mL of ethylene glycol (EG) and sonicated until well dispersed (ca. 4 h). SnF_2 (0.54 g; Aldrich, 7783-47-3) was dissolved in 50 mL of deionized water (DI). $NaBH_4$ (0.51 g; Aldrich, 16940-66-2) dissolved in 50 mL of EG/DI mixture (1:1 by volume) was used as the reducing solution. First, the GnP suspension and SnF_2 solution were combined in a three-neck round-bottom flask and mixed by magnetic stirring with a N_2 gas purge through the mixture for 15 min to remove any dissolved oxygen. Magnetic stirring and N_2 purge continued throughout the duration of the synthesis. After mixing and deaerating, the reaction mixture (GnP and SnF_2) was heated to 55 °C. Once the temperature stabilized, freshly prepared reducing solution was added at a rate of ca. 2 mL/min. The temperature was maintained at 55 °C during addition of the reduction solution and also for 30 min after $NaBH_4$ addition. The reaction mixture was then cooled to room temperature, centrifuged, and washed three times with 0.1 M NaH_2PO_4 in DI, to prevent oxidation in air. The resulting sample was then dried under vacuum.

Electrochemical Characterization. Electrodes for electrochemical characterization were casted onto a 0.03 mm thick copper foil current collector from a suspension of 85:15 wt % $Sn_3O_2(OH)_2$/GnP and poly(vinylidene fluoride) binder (Aldrich, 24937-79-9), respectively, in 0.40 mL of 1-methyl-2-pyrrolidinone (Aldrich, 872-50-4) per gram of solid. The suspension was sonicated and mechanically mixed for over 24 h. The suspension was then applied to copper foil and dried in air on a hot plate until the solvent had evaporated. The deposition density of active material was determined through

DOI: 10.1021/cm504101h
Chem. Mater. 2015, 27, 574−580

measuring the total change in mass after deposition and normalizing per surface area of deposition. The surface area of the electrode is determined by taking a photograph of the sample alongside a ruler, then computing the area using ImageJ[38] software with the scale of pixel/cm calibrated by measurement of the imaged ruler. Using the surface area and density of the deposition, the mass of active material can be determined for each electrode regardless of its size or shape. All electrochemical measurements presented in this paper were conducted utilizing the same electrode deposition, ensuring consistent mass normalization and direct comparison of performance.

All electrochemical measurements were conducted in pouch cells prepared and tested inside an inert Ar atmosphere glovebox (VAC). In the pouch cell assembly, working $Sn_3O_2(OH)_2$/GnP electrodes and counter/reference Li metal foil electrodes were separated by a porous glass filter that had been soaked in commercial 1 M $LiPF_6$ in ethylene carbonate/ethyl methyl carbontate electrolyte (JGHITEC, JC-03-A). Stainless steel strips were used to connect the potentiostat to the pouch cell electrodes by attaching one to the lithium and the other to the copper substrate of the $Sn_3O_2(OH)_2$/GnP anode. The assembly was then placed into a polyethylene pouch and sealed with a thermal impulse sealer. To ensure good contact between the pouch cell components, pressure was applied to both sides of the pouch. Electrochemical characterization was conducted using an EzStat Pro potentiostat/galvanostat (Nuvant Systems, Inc.). Cyclic voltammetry (CV) curves were measured at a rate of 0.1 mV/s in a potential window of 0.01−1.5 V vs Li/Li^+. All charge/discharge curves were measured galvanostatically within the same potential limits.

Materials Characterization. Scanning electron microscopy (SEM; Hitachi S-4700) was used to study the morphology and distribution of $Sn_3O_2(OH)_2$ nanoparticles on GnP. X-ray diffraction (XRD) spectra were taken using a Bruker D2 diffractometer with Cu Kα X-ray source, LynxEye postition-sensitive detector, and accompanying DIFFRACPlus control software. Spectra were taken between 5 and 100 with step size of 0.02 in 2θ. Using PDF4+ software, the background and the Cu $K\alpha_{II}$ contribution were removed. The diffractograms were normalized such that the intensity of the tallest diffraction peak is 100. Both $Sn_3O_2(OH)_2$/GnP and bare GnP powders were measured for comparison.

XAS spectra were acquired at the Materials Research Collaborative Access Team (MRCAT) beamline, Sector 10-BM, of the Advanced Photon Source at Argonne National Laboratory. All samples were measured in transmission mode at the Sn K-edge (29.2 keV) with a reference Sn foil measured simultaneously for proper alignment of multiple scans. For in situ tests, a custom sample chamber[39] was used to ensure the pouch cell was under inert atmosphere by flowing He through the sealed chamber, and that pressure was properly applied using thin polyether ether ketone (PEEK) plates to ensure electrical contact of all components of the pouch cell while not degrading the X-ray signal. A picture of the sample chamber is presented in Figure 1 of the Supporting Information. A pouch cell for in situ XAS experiments was assembled and mounted into the sample chamber inside an Ar atmosphere glovebox (VAC). During the in situ XAS experiment, the $Sn_3O_2(OH)_2$/GnP electrode was charged/discharged galvanostatically for two cycles at a rate of C/2.5 (322 mA/g) and then for two more cycles at C/7.5 (107 mA/g). XAS measurements were taken at initial open-circuit voltage (OCV) and then charged state (0.01 V vs Li/Li^+) and discharged state (1.5 V vs Li/Li^+), where the potentials were held at the respective value to acquire a sufficient number of XAS scans (ca. 2 h). Because of limitations presented by in situ XAS experiments, it is possible for the performance of the electrochemical cells to deviate slightly from that measured in the better controlled environment of the glovebox. This is primarily caused by the reduced pressure applied to the pouch cell components as the thicknesses of the materials for the in situ sample chamber are limited by X-ray absorption cross section.

XAS Data Analysis. The EXAFS spectra were aligned, merged, and normalized using Athena.[40,41] The built-in AUTOBK algorithm was used to minimize background below R_{bkg} = 1.0 Å. Each spectrum was fit using Artemis with theoretical models of $Sn_3O_2(OH)_2$[42] and β-Sn metal,[43] as well as a model based on the $Li_{22}Sn_5$ structure[44] created by FEFF6.[40,41] All spectra were fit using a k range of 2−10 A^{-1}, dk = 3, and fit simultaneously using k, k^2, and k^3 weighting with an R-range of 1−3.3 Å. The OCV spectrum was fit using the Sn−O path of the $Sn_3O_2(OH)_2$ crystal structure. The first charged spectrum was fit using both a Sn−O path and a $Li_{22}Sn_5$-based structure, and all subsequent spectra were fit using Sn−O, Sn−Li, and Sn−Sn contributions. The Sn−Li model is a simplified version of the $Li_{22}Sn_5$ crystal structure, which uses three Sn−Li paths determined by enumerating all the possible Sn−Li near-neighbor distances in the $Li_{22}Sn_5$ structure (four inequivalent Sn sites with an average of ~14 Li near neighbors each) and choosing three distances that represent the most numerous clusters of Sn−Li distances (i.e., 2.7, 3.0, and 3.3 Å). The number of Sn−Li near neighbors, distances, and σ^2 values were determined from fitting the first charged spectrum and then were set for the subsequent fits by only permitting the total number of Sn−Li near neighbors to vary (representing the percent change in the "fully charged" lithiated state).

RESULTS AND DISCUSSION

Figure 1a shows XRD of $Sn_3O_2(OH)_2$/GnP, base GnP, and the $Sn_3O_2(OH)_2$ standard.[42] Nearly all diffraction peaks of

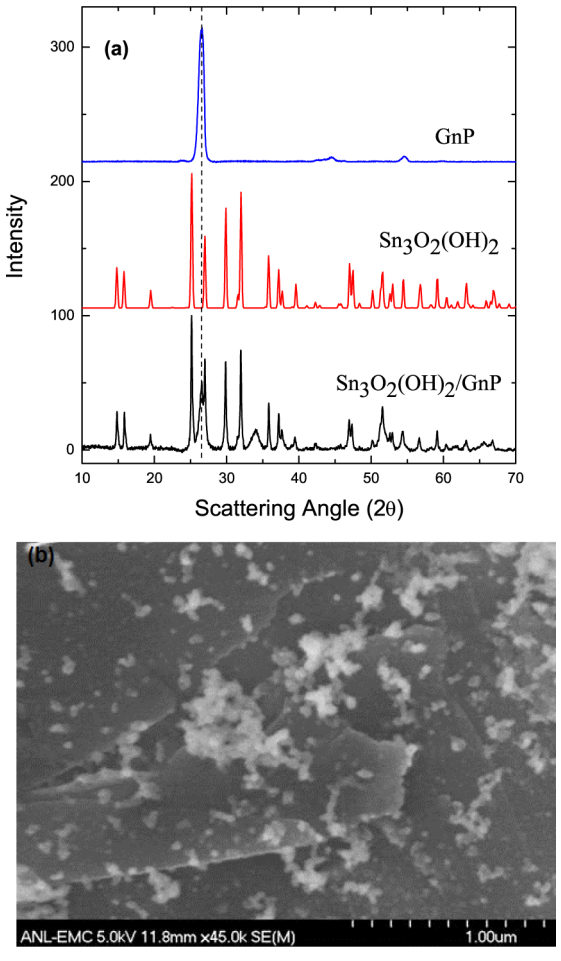

Figure 1. (a) XRD for $Sn_3O_2(OH)_2$/GnP, $Sn_3O_2(OH)_2$,[42] and GnP and (b) SEM images of as-synthesized $Sn_3O_2(OH)_2$/GnP.

$Sn_3O_2(OH)_2$/GnP are attributable to the standard crystalline phase of $Sn_3O_2(OH)_2$ with the exception of a broad peak at ca. 34° corresponding to a slight contribution of an SnO_x phase. The peak at 26.5° is from GnP and is marked by the vertical dashed line in Figure 1a. Using the Scherrer equation,[45] the crystallite sizes of $Sn_3O_2(OH)_2$ are estimated to be 40−50 nm. SEM images of $Sn_3O_2(OH)_2$/GnP composite (Figure 1b)

DOI: 10.1021/cm504101h
Chem. Mater. 2015, 27, 574−580

confirm a particle size of ca. 50 nm along with a homogeneous distribution on the surface of the GnP particles.

CV curves of $Sn_3O_2(OH)_2$/GnP electrode (Figure 2a) show reversible peaks at ca. 0.2 and 0.65 V, attributable to Li

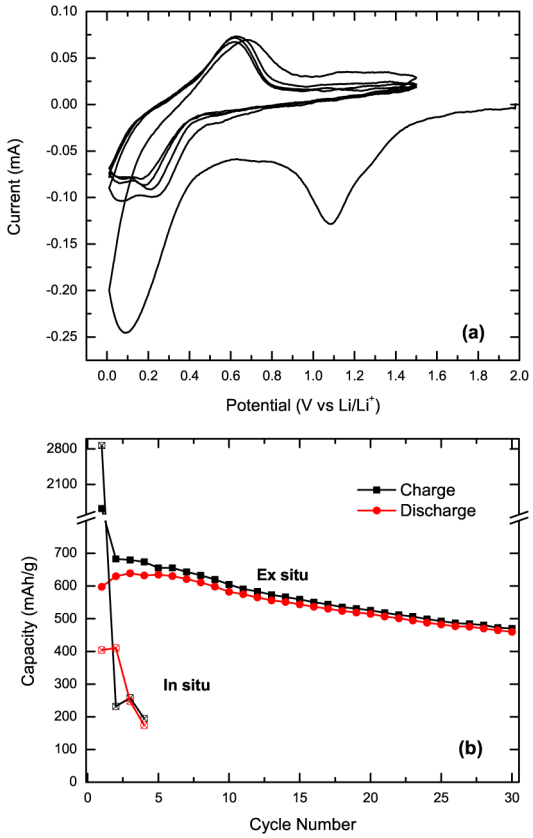

Figure 2. Electrochemical characterization of $Sn_3O_2(OH)_2$/GnP electrodes: (a) CVs at 0.1 mV/s between 0.01 and 1.5 V vs Li/Li^+ and (b) glovebox tested capacity performance up to 30 cycles at *C*/4 rate (solid points) and in situ performance at *C*/2.5 and *C*/7.5 rates (hollow points).

insertion and deinsertion, respectively, are similar to the features observed with cyclic voltammetry on SnO and SnO_2 electrodes.[10] The first CV curve is significantly different than the following cycles due to the irreversible conversion of oxygen from tin oxide to Li_2O (peak at ca. 1.1 V), as well as formation of solid electrolyte interface (SEI) (broad peak starting at ca. 0.4 V). Assuming all tin from the synthesis has precipitated onto the GnP (93 wt % $Sn_3O_2(OH)_2$ and 7 wt % GnP), the theoretical capacity of this composite is 755 mAh/g. Figure 2b shows the capacity of cycled $Sn_3O_2(OH)_2$/GnP at *C*/4 rate (166 mA/g) for 30 cycles in a pouch cell similar to the one used for the in situ experiment, with the difference that the cell remained inside an Ar glovebox throughout the test, firmly clamped between two solid PEEK plates. The second cycle shows a reversible charging capacity of 683 mAh/g, and by the 30th cycle the capacity decreases to 470 mAh/g, i.e., a 31% drop. Figure 2b also displays the capacity exhibited with the in situ pouch cell. The lower capacity is a combined result of the limitations of in situ experiments discussed previously, faster charging rate (*C*/2.5 compared to *C*/4 initially) and accelerated structural degradation as suggested by the EXAFS analysis.

The results from the in situ EXAFS study of $Sn_3O_2(OH)_2$/GnP electrode at open circuit voltage (OCV), first charged state, and first discharged state are presented in Figure 3 as *R*-space plots (Fourier transforms of $k^2\chi(k)$). The peak heights

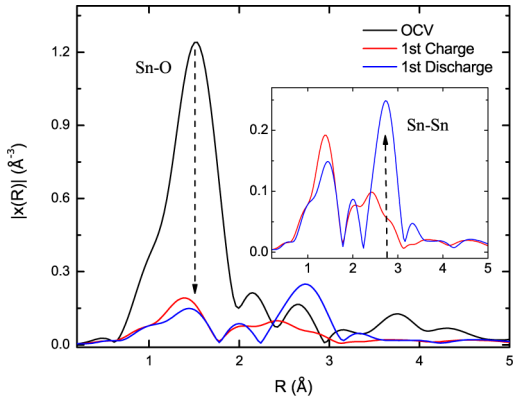

Figure 3. $|\chi(R)|$ of OCV, first charge state, and first discharge state. Inset shows zoomed-in view of first charge and discharge data.

and positions are related to (but do not directly indicate) the number of nearest neighbors and atomic distances, respectively. A clear change in local tin structure is observed between OCV and the first charged state. The intensity of the Sn−O peak at ca. 1.4 Å is reduced while a broad peak between 1.7 and 3.0 Å evolves as shown in the inset of Figure 3. After the first discharge the latter broad peak evolves into a new distinct peak at ca. 2.8 Å. This transition between charged and discharged spectra is similar in the remaining cycles. The peak at 2.8 Å was successfully modeled with a shifted β-Sn metal structure, and the broad peak between 1.7 and 3.0 Å is a convolution of several Sn−Li peaks (modeled by three paths as described above). Initially, all discharged states were fit with only Sn−O and Sn−Sn contributions; however, this model left a large residual signal around 2.5 Å, particularly at lower *k*-weights. Including Sn−Li path contributions based on the Sn−Li model determined from the first charged spectrum resulted in greatly improved fits. Example fits in $k^2\chi(k)$, $Re[\chi(R)]$, and $|\chi(R)|$ are presented for the first charged spectrum (Figure 4) and first discharged spectrum (Figure 5). The Sn−Li contributions determined from fitting are also shown in $|\chi(R)|$ as blue dotted lines. Clearly Sn−Li paths cannot be ignored as they significantly contribute to the $|\chi(R)|$ between 1.7 and 3.0 Å. Fitting results for all spectra can be found in Figure 2 in the Supporting Information.

In addition to structural changes seen in the EXAFS, there are also distinct changes in the form of XANES shifts shown in Figure 3 in the Supporting Information. A large shift is seen from OCV (oxidized state) to metallic Sn on first charge. Subsequent charge/discharge do not show large shifts, which suggests limited changes in oxidation state during further cycling. This trend is also seen in the EXAFS data.

Near-neighbor fitting and atomic distance results for Sn−O and Sn−Sn are shown in Figure 6. The OCV spectrum fits well with the $Sn_3O_2(OH)_2$ structure[42] with 4.2 ± 0.3 Sn−O near neighbors. After the first charge, the Sn−O environment decreases to 0.6 ± 0.1 near neighbors. In the following charge and discharge cycles, the number of Sn−O near neighbors continues to decrease but at a much slower rate.

After the first discharge cycle, the two Sn−Sn paths are observed in all the following states (Figure 6). Distances in both Sn−Sn paths oscillate and get shorter in the discharged state and longer in the charged state, which correlates to

DOI: 10.1021/cm504101h
Chem. Mater. 2015, 27, 574−580

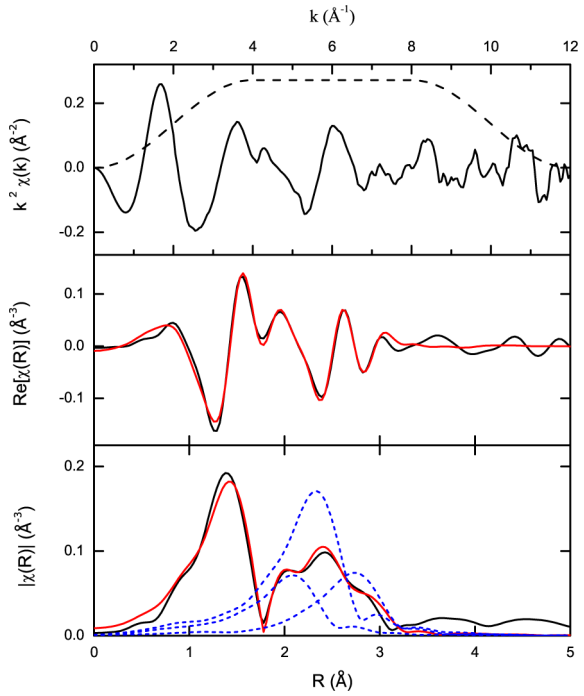

Figure 4. $k^2\chi(k)$, $Re[\chi(R)]$, and $|\chi(R)|$ for first charged state. The black line represents the data, the red line represents the fit, and the blue dotted lines are the magnitudes of the Sn−Li contributions determined from fitting. The Fourier transform window in *k*-space is shown in the top panel.

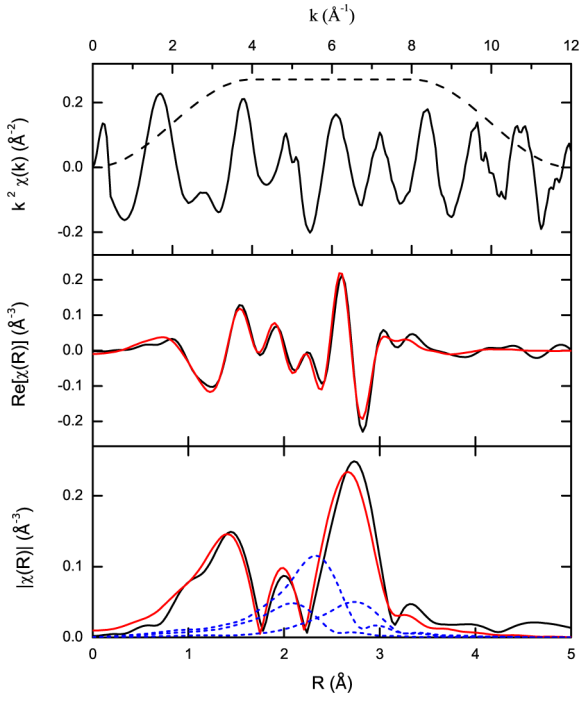

Figure 5. $k^2\chi(k)$, $Re[\chi(R)]$, and $|\chi(R)|$ for the first discharged spectra. The black line represents the data, the red line represents the fit, and the blue dotted lines are the magnitudes of the Sn−Li contributions determined from fitting. The Fourier transform window in *k*-space is shown in the top panel.

lithiation/delithiation of metallic tin. For example, the closer of the two Sn−Sn near neighbors has a distance of 2.88 ± 0.01, 2.89 ± 0.01, and 2.90 ± 0.01 Å for the first, second, and third

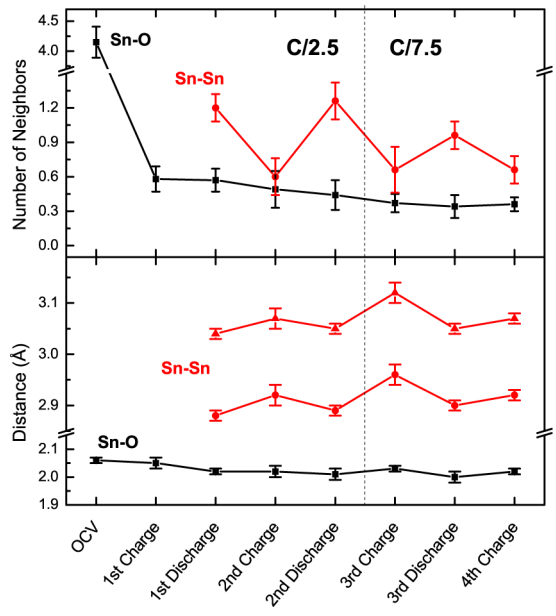

Figure 6. Number of nearest-neighbor and atomic-distance results from EXAFS fitting for Sn−O and Sn−Sn.

discharges, respectively, and in the charged (lithiated) state, the Sn−Sn distance expands to 2.92 ± 0.02 Å on the second cycle and to 2.96 ± 0.02 Å on the third cycle. This is also reflected in the oscillating number of Sn−Sn neighbors, decreasing in a charged state (0.6 ± 0.2 on first charge) and increasing in a discharged state (1.2 ± 0.1 on first discharge). This implies a swelling and relaxing type of behavior of the metallic Sn clusters due to Li insertion, i.e., the Sn−Sn distances must increase to accommodate the inserted Li when charging and relax back upon Li removal on discharge.

Besides changes in Sn−O paths, the first charged state contains multiple Sn−Li paths. Using the simplified $Li_{22}Sn_5$ model outlined above, three Sn−Li distances of 2.65 ± 0.08, 2.90 ± 0.06, and 3.32 ± 0.09 Å were used in the model and resulted in 1.6 ± 0.3, 5.1 ± 0.8, and 4.2 ± 0.9 near neighbors, respectively (Figure 7). These distances are close to the most common Sn−Li distances found in $Li_{22}Sn_5$ (i.e., ca. 2.70, 3.00, and 3.30 Å) with the expected relative ratio of Sn−Li near neighbors at each distance.

It should be noted that all but OCV spectra have statistically significant Sn−Li contributions, even in the discharged states (Figure 7). The first charged state has 10.9 ± 1.2 Li near neighbors, and the following discharged state has 7.3 ± 1.0 Li near neighbors, with the second and third cycles following the same trend. Irreversible insertion of Li on the first cycle correlates with the low capacities exhibited for in situ samples, suggesting a large amount of the initially inserted Li is not removed upon discharge. The charge rate on the first and second cycles was C/2.5 (as calculated from theoretical capacity values) and was reduced to C/7.5 on the third and fourth cycles. As has been previously discussed,[46,47] the charge rate has a large impact on the observed capacity, i.e., the faster the charging rate, typically the lower is the capacity. The performance did not change significantly when the slower charge rate was applied; the number of Sn−Li near neighbors for the third charged state was 12.0 ± 1.4, which is within the fit error compared with the first charged state. If all the tin had been converted to the $Li_{22}Sn_5$ structure, we would expect a total of ca. 14 Sn−Li near neighbors. Therefore, it can be concluded

DOI: 10.1021/cm504101h
Chem. Mater. 2015, 27, 574−580

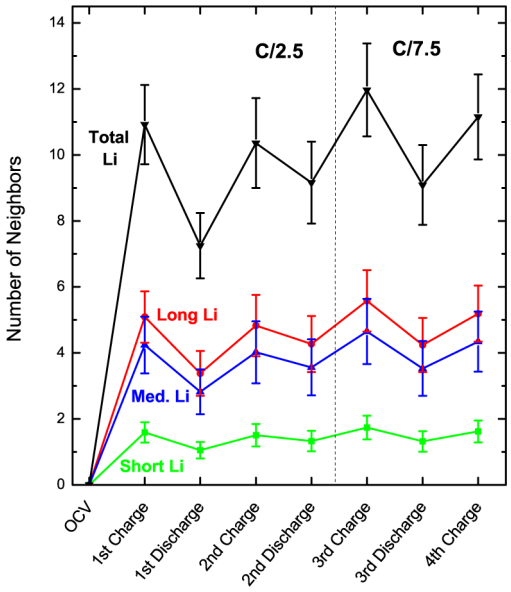

Figure 7. Sn−Li near-neighbor behavior as determined from EXAFS fitting.

that a mixture of active and inactive anode material was present in the in situ electrode due to cycling degradation. If a portion of the electrode was initially inactive, the EXAFS would reflect a portion of the OCV spectrum in all subsequent fits, which is not observed.

The electrochemical performance of our in situ pouch cell showed accelerated capacity degradation compared to pouch cells prepared using the same electrode deposition but kept more firmly clamped in a glovebox rather than mounted in the in situ chamber. To verify that the capacity fading is indeed related to the structural changes in the anode material, we have compared the EXAFS results from the in situ cell to EXAFS measured ex situ on an electrode extracted from a pouch cell that had been cycled inside the glovebox for 10 cycles and showed slow capacity fading. On the last discharge cycle before extraction, the electrode material showed capacity of 400 mAh/g. Figure 4 in the Supporting Information compares both in situ and ex situ EXAFS in *R*-space, which display the same structural changes. This strongly suggests the lower capacity observed during in situ measurements is a result of irreversible structural changes occurring during charge and discharge cycling within the electrode material and can be extrapolated to a general degradation mechanism of these materials.

Our experimental results are in agreement with previous studies,[30,32,34] where a consistent Sn−O path exists throughout all spectra and the number of Sn−O near neighbors drastically drops after the first charge, and then both the number of Sn−O neighbors and the atomic distance gradually decrease in the following charge/discharge cycles. Combining this finding and the emergence of metallic β-Sn structure on the first discharge suggests metallic Sn domains are embedded in an amorphous Li_2O matrix after the first charge, which is also seen in TEM by Nie et al.[36] After the formation of these clusters, there is a presence of Sn−Sn neighbors in both charged and discharged spectra. This suggests that, past the first charge, not all of the Sn is participating in the lithiation reaction.

On the basis of our experimental results, the following mechanism due to cycling can be proposed to explain capacity fading in the studied anode material. The $Sn_3O_2(OH)_2$ crystal structure consists of clusters of six tin and eight oxygen, with each cluster positioned in a body-centered cubic unit cell geometry. The EXAFS fitting results suggest that, upon first charge, these clusters are distorted so that tin atoms shift toward the center of each cluster, forming metallic tin clusters while oxygen is mostly converted to amorphous Li_2O and LiOH species, which are segregated on a periphery of the metallic tin. In subsequent cycles higher levels of Sn and Li_2O segregation are achieved as the number of Sn−O near neighbors decreases and the tin clusters expand and contract as Li is inserted and removed as illustrated in the graphical abstract to this paper. The capacity fading can be explained by each of the atomic clusters eventually losing electrical contact with the neighboring clusters. This is supported by the presence of Sn−Li paths even in discharged states, meaning the cluster was in electrical contact initially, but once the conversion of the oxygen to the Li_2O shell is completed and the shift of tin atoms to the center of the cluster occurs, it becomes electrically insulated from the rest of the electrode and thus retains Li in the tin cluster core as it can no longer participate in electrochemical reactions. This is a different mechanism than the one previously suggested for SnO_x compounds,[5−8] where the capacity fading is attributed to expansive volumetric changes. In this $Sn_3O_2(OH)_2$ structural degradation model, the tin volumetric expansions are reversible as shown in the changes in Sn−Sn distances after the first charge (Figure 6). Rather, the mechanism is based on segregation of phases during cycling, converting the initial tin oxyhydroxide crystal structure into atomic clusters of tin surrounded by an insulating Li_2O/LiOH shell as dictated by the original crystal structure of $Sn_3O_2(OH)_2$. Thus, although our composite nanomaterials were designed to provide improved electrical conductivity to nanoparticles by depositing them onto the graphite, the cluster-like crystalline structure of $Sn_3O_2(OH)_2$ is the primary limitation of cycle life of this composite anode nanomaterial.

CONCLUSIONS

Analysis of the in situ EXAFS spectra from charged and discharged states of $Sn_3O_2(OH)_2$/GnP anodes provides unique insight into the complex mechanism of Li insertion/removal into the tin oxyhydroxide based anode materials. As was described above, upon the first charge, oxygen from $Sn_3O_2(OH)_2$ converts to Li_2O as shown in the change in Sn−O near neighbors (Figure 6), in agreement with previous studies of tin oxide materials.[30,32,34] During the first charge, the majority of the newly formed metallic tin is converted to a $Li_{22}Sn_5$-type structure, as has been observed previously through in situ XRD measurements on tin oxide.[27] As the cell is charged and discharged, segregation of the atomic clusters of metallic tin surrounded by a Li_2O/LiOH shell is observed. Metallic tin clusters initially are in electrical contact with the rest of the anode and can volumetrically expand and contract as Li is inserted and removed, respectively. This fluctuating change in the structure is seen in the change of Sn−Sn and Sn−Li atomic distances and near neighbors. For the first time in this study, we have been able to use XAS to probe Li insertion into anode materials with quantitative results. As cycling proceeds tin atomic clusters become fully insulated from the rest of the electrode by Li_2O/LiOH shells and stop participating in the electrochemical reaction. The deduced structural degradation mechanism correlates to capacity fading and indicates the inherent limitation of the $Sn_3O_2(OH)_2$ crystal structure to reversible Li insertion. The understanding gained about the

DOI: 10.1021/cm504101h
Chem. Mater. 2015, 27, 574−580

evolution of anode atomic structure during charge/discharge cycles can help design better anode materials, avoiding cluster-like structures for active materials. Future studies involve strategies to improve electrochemical performance of Sn-based anodes, emphasizing the need to facilitate Sn−Li interactions, particularly ensuring the reversibility of Li removal during discharge. In addition, this study has demonstrated how in situ XAS can be used to gain new structural insight on various LIB electrodes.

■ ASSOCIATED CONTENT

Ⓢ Supporting Information

Photos of experimental setup and in situ sample chamber, all EXAFS fits in $k^2\chi(k)$, $Re[\chi(R)]$, and $|\chi(R)|$ along with a table of detailed fitting results, XANES data, and comparison of EXAFS for in situ and ex situ cycled electrodes. This material is available free of charge via the Internet at http://pubs.acs.org/.

■ AUTHOR INFORMATION

Corresponding Author

*E-mail: cpellic1@hawk.iit.edu.

Notes

The authors declare no competing financial interest.

■ ACKNOWLEDGMENTS

C.J.P. was supported by a Department of Education GAANN Fellowship, award no. P200A090137, and the National Science Foundation under Grant no. DMR-086935. The project is supported by U.S. Department of Energy, Office of Basic Energy Science. MRCAT operations are supported by the Department of Energy and the MRCAT member institutions. Use of the Argonne National Laboratory Advanced Photon Source and Electron Microscopy Center is supported by the U.S. Department of Energy, under Contract no. DE-AC02-06CH113.

■ REFERENCES

(1) Reynier, Y. F.; Yazami, R.; Fultz, B. *J. Electrochem. Soc.* **2004**, *151*, A422−A426.
(2) Wang, C.; Li, D.; Too, C.; Wallace, G. *Chem. Mater.* **2009**, *21*, 2604−2606.
(3) Armand, A.; Tarascon, J. M. *Nature* **2008**, *451*, 652−657.
(4) Beaulieu, L. Y.; Ebermand, K. W.; Turner, R. L.; Krause, L. J.; Dahn, J. R. *Electrochem. Solid-State Lett.* **2001**, *9*, A137−A140.
(5) Derrien, G.; Hassoun, J.; Panero, S.; Scrosati, B. *Adv. Mater. (Weinheim, Ger.)* **2007**, *19*, 2336−2340.
(6) Alcantara, R.; Rodriguez, I.; Tirado, J. L. *ChemPhysChem* **2008**, *9*, 1171−1177.
(7) Chamas, M.; Lippens, P. E.; Jumas, J. C.; Boukerma, K.; Dedryvere, R.; Gonbeau, D.; Hassoun, J.; Panero, S.; Scrosati, B. *J. Power Sources* **2011**, *196*, 7011−7015.
(8) Kim, C.; Noh, M.; Choi, M.; Cho, J.; Park, B. *Chem. Mater.* **2005**, *17*, 3297−3301.
(9) Wang, Y.; Sakamoto, J.; Kostov, S.; Mansour, A.; denBoer, M.; Greenbaum, S. G.; Huang, C.-K.; Surampudi, S. *J. Power Sources* **2000**, *89*, 232−236.
(10) Kim, J. H.; Jeong, G. J.; Kim, Y. W.; Sohn, H. J.; Park, C. W.; Lee, C. K. *J. Electrochem. Soc.* **2003**, *150*, A1544−A1547.
(11) Zhang, L.; Jiang, L.; Yan, H.; Wang, W.; Song, W. W. W.; Guo, Y.; Wan, L. *J. Mater. Chem.* **2010**, *20*, 5462−5467.
(12) Huang, X.; Zhou, X.; Zhou, L.; Qian, K.; Wang, Y.; Liu, Z.; Yu, C. *ChemPhysChem* **2011**, *12*, 278−281.
(13) Zhang, M.; Lei, D.; Du, Z.; Yin, X.; Chen, L.; Li, Q.; Wang, Y.; Wang, T. *J. Mater. Chem.* **2011**, *21*, 1673−1676.
(14) Wang, G.; Wang, B.; Wang, X.; Park, J.; Dou, S.; Ahn, H.; Kim, K. *J. Mater. Chem.* **2009**, *19*, 8378−8384.
(15) Li, Y.; Lv, X.; Lu, J.; Li, J. *J. Phys. Chem. C* **2010**, *114*, 21770−21774.
(16) Balan, L.; Schneider, R.; Willmann, P.; Billaud, D. *J. Power Sources* **2006**, *161*, 587−593.
(17) Chen, Y.-C.; Chen, J.-M.; Huang, Y.-H.; Lee, Y.-R.; Shih, H. C. *Surf. Coat. Technol.* **2007**, *202*, 1313−1318.
(18) Liu, B.; Guo, Z. P.; Du, G.; Nuli, Y.; Hassan, M. F.; Jia, D. *J. Power Sources* **2010**, *195*, 5382−5386.
(19) Yao, J.; Shen, X.; Wang, B.; Liu, H.; Wang, G. *Electrochem. Commun.* **2009**, *11*, 1849−1852.
(20) Kim, H.; Kim, S.-W.; Park, Y.-U.; Gqon, H.; Seo, D.-H.; Kim, Y.; Kang, K. *Nano Res.* **2010**, *3*, 813−821.
(21) Wang, D.; Li, X.; Yang, J.; Wang, J.; Geng, D.; Li, R.; Cai, M.; Sham, T. K.; Sun, X. *Phys. Chem. Chem. Phys.* **2013**, *15*, 3535−3542.
(22) Wang, G.; Ahn, J.-H.; Lindsay, M. J.; Sun, L.; Bradhurts, D. H.; Dou, S. X.; Liu, H. K. *J. Power Sources* **2001**, *97*−*98*, 211−215.
(23) Du, Z.; Yin, X.; Zhang, M.; Hao, Q.; Wang, Y.; Wang, T. *Mater. Lett.* **2010**, *64*, 2076−2079.
(24) Lin, J.; Peng, Z.; Xiang, C.; Ruan, G.; Yan, Z.; Natelson, D.; Tour, J. M. *ACS Nano* **2013**, *7*, 6001−6006.
(25) Chouvin, J.; Branci, C.; Sarradin, J.; Oliver-Fourcade, J.; Jumas, J. C.; Simon, B.; Biensan, P. *J. Power Sources* **1999**, *81*−*82*, 277−281.
(26) Poizot, P.; Laruelle, S.; Grugeon, S.; Dupont, L.; Tarascon, J.-M. *Nature* **2000**, *407*, 496−499.
(27) Rhodes, K. J.; Meisner, R.; Kirkham, M.; Dudney, N.; Daniel, C. *J. Electrochem. Soc.* **2012**, *159*, A294−A299.
(28) Chouvin, J.; Vicente, C. P.; Oliver-Fourcade, J.; Jumas, J.-C.; Simon, B.; Biensan, P. *Solid State Sci.* **2004**, *6*, 39−46.
(29) Connor, P.; Irvine, J. *Electrochim. Acta* **2002**, *47*, 2885−2895.
(30) Mansour, A. N.; Mukerjee, S.; Yang, X. Q.; McBreen, J. *J. Synchrotron Radiat.* **1999**, *6*, 596−598.
(31) Zhang, W.; Duchesne, P.; Gong, Z. L.; Wu, S. Q.; Ma, L.; Jiang, Z.; Zhang, S.; Zhang, P.; Mi, J. X.; Yang, Y. *J. Phys. Chem. C* **2013**, *117*, 11498−11505.
(32) Chouvin, J.; Oliver-Fourcade, J.; Jumas, J. C.; Simon, B.; Biensan, P.; Madrigal, F. J. F.; Tirado, J. L.; Vicente, C. P. *J. Electroanal. Chem.* **2000**, *494*, 136−146.
(33) Jung, H. R.; Lee, W. J. *J. Electroanal. Chem.* **2011**, *662*, 334−342.
(34) Goward, G. R.; Leroux, F.; Power, W. P.; Ouvrard, G.; Dmowski, W.; Egami, T.; Nazar, L. F. *Electrochem. Solid-State Lett.* **1999**, *2*, 367−370.
(35) Yoon, S.; Lee, J. M.; Kim, H.; Im, D.; Doo, S. G.; Sohn, H. J. *Electrochim. Acta* **2009**, *54*, 2699−2705.
(36) Nie, A.; Gan, L.-Y.; Cheng, Y.; Asayesh-Ardakani, H.; Li, Q.; Dong, C.; Tao, R.; Mashayek, F.; Wang, H.-T.; Schwingenschlogl, U.; Klie, R. F.; Yassar, R. S. *ACS Nano* **2013**, *7*, 6203−6211.
(37) Zhong, L.; Liu, X. H.; Wang, G. F.; Mao, S. X.; Huang, J. Y. *Phys. Rev. Lett.* **2011**, *106*, 248302.
(38) Abramoff, M. D.; Magalhaes, P. J.; Ram, S. J. *Biophotonics Int.* **2004**, *11*, 36−42.
(39) Pelliccione, C.; Timofeeva, E.; Katsoudas, J.; Segre, C. *Rev. Sci. Instrum.* **2014**, *84*, 126108.
(40) Ravel, B.; Newville, M. *J. Synchrotron Radiat.* **2005**, *12*, 537−541.
(41) Newville, M. *J. Synchrotron Radiat.* **2001**, *8*, 322−324.
(42) Abrahams, I.; Grimes, S. M.; Johnstons, S. R.; Knowles, J. C. *Acta Crystallogr., Sect. C: Cryst. Struct. Commun.* **1996**, *52*, 286−288.
(43) Swanson, H. E.; Tatge, E. *Natl. Bur. Stand. (U.S.)* **1953**, *539*, 1−95.
(44) Gladyshevskii, E. I.; Oleskiv, G. I.; Kripyakevich, P. I. *Sov. Phys., Crystallogr.* **1964**, *9*, 269−271.
(45) Patterson, A. *Phys. Rev.* **1939**, *56*, 978−982.
(46) Alcantara, R.; Nwokeke, U.; Rodriguez, I.; Tirado, J. *Electrochem. Solid-State Lett.* **2008**, *11*, A209−A213.
(47) Brassart, L.; Zhao, K.; Suo, Z. *Int. J. Solids Struct.* **2013**, *50*, 1120−1129.

DOI: 10.1021/cm504101h
Chem. Mater. 2015, 27, 574−580